

Metal-Organic Framework Thin Films with Diverse Redox-Active/Inactive Components for Enhanced Optical Modulation and Coloration Efficiency

Shuai Feng^a, Junxin Wang^b, Zhangfa Tong^a and Hui-Ying Qu^{a, *}

Shuai Feng and Junxin Wang contributed equally to this work.

^aGuangxi Key Laboratory of Petrochemical Resource Processing and Process Intensification Technology, School of Chemistry and Chemical Engineering Guangxi University, Nanning 530004, China

^bDepartment of Materials Science and Metallurgy, University of Cambridge, 27 Charles Babbage Road, Cambridge CB3 0FS, United Kingdom

*Corresponding author. E-mail: huiying.qu@gxu.edu.cn

Highlights

- The redox and coloration mechanisms of different MOFs are reported.
- Co²⁺ doping into Cu-TCA for substitution of Cu²⁺ was firstly reported.
- The Co/Cu-TCA film exhibits high optical modulation and coloration efficiency.

Abstract

Electrochromism is attractive due to the increasing demand for intelligent devices such as smart windows and display apparatuses. Metal-organic frameworks (MOFs) are found to be promising electrochromic materials thanks to their tailorable structures and chemical compositions via combining various metal centers and organic ligands. However, the uncovered redox mechanism, the insulating and inactive redox nature for majority of MOFs have hampered their practical application as efficient electrochromic materials. Herein, four MOF thin films (Cu-TCA, Zn-TCA, HKUST-1 and Zn-MOF-74) constructing from redox-active/inactive metal centers and organic ligands were prepared, and their electrochromic performance in a Li-ion-conducting electrolyte was present. We demonstrate that redox-active metal centers and organic ligands in MOFs contribute to the reversible and sustainable optical modulation. A further investigation was carried out to dope redox-active metal center Co^{2+} into the Cu-TCA thin film, serving as the second metal center. Unambiguous evidence shows that Co^{2+} doping can enlarge the specific surface area and pore volume of Cu-TCA to facilitate the transport and intercalation/deintercalation of ions and electrons, resulting in the enhanced transmittance modulation (70% at 705 nm) and coloration efficiency ($337 \text{ cm}^2 \cdot \text{C}^{-1}$). Our work provides an important approach and guidance in designing efficient MOFs for electrochromic application.

Keywords: Electrochromism, Metal-organic frameworks, Bi-metal centers, Redox-active, Co/Cu-TCA thin film

1. Introduction

The rapid development of intelligent optoelectronic devices has triggered an upsurge of researches. Their optical properties can be varied synchronously with the electrochemical signal, and vice versa. Thus, the electrochemical signal applied on the optoelectronic materials can be visually judged by their optical performance [1]. The change in appearance color in response to outer stimuli, also known as chromogenic behavior, is well suit to the concept of intelligent technology. It includes electrochromism, thermochromism, photochromism and gasochromism, and has been proposed and extensively investigated in recent decades [2-5]. Among these, electrochromism is more maneuverable and has been commercialized due to its superior performance. Electrochromism refers to a phenomenon whereby a material reversibly and persistently changes its optical properties (transmittance, reflectance, and absorbance) via redox reactions resulting from intercalation/deintercalation of ions and electrons by applying a small electric signal, and has been widely used in smart windows, dimming mirrors, displays and camouflage objects [6, 7]. Decades of research investigating electrochromism have led to significant progress in this field, various types of electrochromic (EC) materials including transition metal oxides [8-10], coordination compounds [11], small organic molecules [12] and conducting polymers [13] have been developed. However, for the former two types, the range of available colors and brightness are limited, while the latter twos suffer from low UV protection index and electrochemical stability. To improve the performance of the known EC materials, morphology and nanostructure are generally modified by constructing more pores and channels to expose larger surface areas, thus creating more active sites for redox reactions. Such approaches can enhance transition efficiencies and reaction rates of ions and electrons, leading to fast response, high coloration efficiency and long-term durability [14-16]. Wang et al. reported MOF-derived NiO@C films with a hierarchical-porous structure through two-step pyrolysis,

which showed a rapid color switch between transparent and brown, high coloration efficiency ($113.5 \text{ cm}^2 \cdot \text{C}^{-1}$) at 550 nm and ultra-stable EC cycles [17]. However, the complicated methods for surface/structure engineering and the cost incurred have hampered their applications.

The recent development of versatile metal-organic frameworks (MOFs) provides an intriguing opportunity for the study of their applications in electrochromism [18, 19] (Fig. 1a). MOFs, a new class of porous crystalline materials, are constructed from metal centers and organic ligands with unique microporous structure, large specific surface area, and tunable redox-active sites [20]. MOFs are ideal for electrode materials due to their tailorable structures at the molecular level and small volume change during the electrochemical reactions. D'Alessandro et al. demonstrated a new potential through-space mechanism for charge transfer in MOFs, providing theoretical support to promote the application of MOFs in redox reactions [21]. Wang et al. fabricated Ni-CHNDI MOF thin films with a big channel size ($\sim 33 \text{ \AA}$), exhibiting high optical contrast (73%), high coloration efficiency ($260 \text{ cm}^2 \cdot \text{C}^{-1}$) at 720 nm and good electrochemical stability in the Na^+ -based electrolyte [22]. Moreover, the type of redox-active/inactive metal centers and organic ligands in MOFs regulate the redox activity, specific surface area and pore structure, thus affecting the diffusion and intercalation/deintercalation of ions in the electrolyte and the transition of electrons. Therefore, rational selection of redox-active/inactive metal centers and organic ligands for MOFs are significant. Two strategies are commonly used to improve the pore structure of MOFs. The first one is to incorporate ligands with longer chains, or alter sidechain substitutions. However, it relies on organic synthesis and modification of the ligands, and the resulting MOFs' pores are not large enough [23]. The second one is to incorporate other metal ions, which was proved to be a feasible approach [24]. Therefore, an important frontier in MOFs used as electrode materials is the rational design of the composition and structure by using different metal centers and organic ligands. Various

metal centers (Cu, Zn, Ni, etc.) and organic ligands (2,5-dihydroxyterephthalic acid (H_4dobdc), 4,4',4''-tricarboxytriphenylamine (H_3TCA), 1,3,5-benzotri-carboxylic acid (H_3BTC), etc.) have been successfully adopted for constructing MOFs [25-30] (Fig. 1b). It is suggested that the MOFs containing redox-active organic ligands exhibit EC performance [31, 32]. Recent work of Issam Mjejri et.al has pointed out that metal centers can also have a positive impact on the EC properties of MOFs [33]. Therefore, in order to promote the EC performance of MOFs, it is necessary to investigate the combined effect of metal centers and organic ligands, their microporous structures and specific surface area, which determine the transport and intercalation/deintercalation rate of ions and electrons during the EC process.

Herein, EC processes of five MOFs comprising of redox active/inactive metal centers and organic ligands in the Li^+ -based electrolyte were given. The coloration mechanism of four MOF thin films during EC process was first studied, they are (i) Cu-TCA containing the redox-active metal center Cu(II) and organic ligand TCA^{3-} , (ii) Zn-TCA containing the redox-inactive metal center Zn(II) and the redox-active organic ligand TCA^{3-} , (iii) HKUST-1 containing the redox-active metal center Cu(II) and the redox-inactive organic ligand BTC^{3-} , and (iv) Zn-MOF-74 containing the redox-inactive metal center Zn(II) and organic ligand $dobdc^{4-}$. A further study of Co/Cu-TCA with enhanced EC performance was also presented, the redox-active metal center Co(II) was doped into Cu-TCA to increase the specific surface area and pore volume, and the electrochemical activity of Co(II) doping was highlighted.

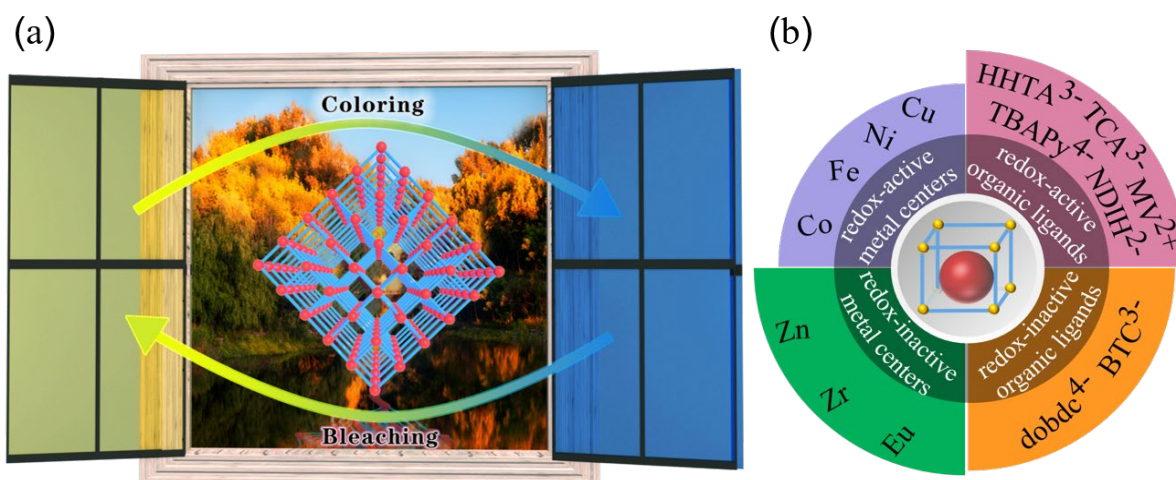


Fig. 1. (a) Schematic illustration of the MOFs-based EC smart window, (b) examples of redox active and inactive metal centers and organic ligands forming MOFs.

2. Experimental section

2.1. Reagents and chemicals

Potassium sulfate (K_2SO_4 , 99.0%), trisodium citrate dihydrate ($\text{C}_6\text{H}_5\text{Na}_3\text{O}_7 \cdot 2\text{H}_2\text{O}$, 99.0%), N, N-dimethyl foramide ($\text{C}_3\text{H}_7\text{NO}$, 99.9%), sodium sulfate anhydrous (Na_2SO_4 , 99.0%), sodium hydroxide (NaOH , 96.0%), sodium lauryl sulfate ($\text{C}_{12}\text{H}_{25}\text{SO}_4\text{Na}$, 97.0%), hexane ($\text{CH}_3(\text{CH}_2)_4\text{CH}_3$, 97.0%) and cobalt chloride hexahydrate ($\text{CoCl}_2 \cdot 6\text{H}_2\text{O}$, 99.0%) were purchased from Guangdong Guanghua sci-Tech Co., Ltd. 4,4',4''-tricarboxytriphenylamine ($\text{C}_{21}\text{H}_{15}\text{NO}_6$, 98.0%) and tetrabutylammonium perchlorate ($\text{C}_{16}\text{H}_{36}\text{ClNO}_4$, 98.0%) were purchased from Sigma-Aldrich. Copper(II) sulfate anhydrous (CuSO_4 , 99.0%), ethanol ($\text{C}_2\text{H}_5\text{OH}$, 99.5%), acetone ($\text{C}_4\text{H}_6\text{O}$, 99.5%), lithium perchlorate (LiClO_4 , 95.0%) and propylene carbonate ($\text{C}_4\text{H}_6\text{O}_3$, 99.7%) were purchased from Sinopharm Chemical Reagent Co., Ltd. HKUST-1 and Zn-MOF-74 were purchased from Xi'an Ruixi Biological Technology Co., Ltd. Conductive indium tin oxide (ITO)-coated glass substrates with a resistance of $6 \Omega \cdot \text{sq}^{-1}$ were obtained from Advent South China Xiang Science and Technology. All chemicals were used without any further purification.

2.2. Preparation of the MOF thin films

ITO-coated glass substrates were ultrasonically cleaned in acetone, ethanol, and distilled water for 15 min each and dried in a vacuum oven for further use. Cu-TCA, Zn-TCA, and Co/Cu-TCA thin films were prepared at room temperature using a Chenhua CHI760E electrochemical workstation with a conventional three-electrode system. The ITO-coated glass, Ag/AgCl and a platinum sheet were used as working electrode, reference electrode and counter electrode, respectively. Cu-TCA, Zn-TCA, and Co/Cu-TCA thin films were synthesized via electrodeposition followed by electro-oxidation. The schematic illustration of electrodeposition and electro-oxidation processes of MOFs thin films was shown in Fig. S1.

Cu-TCA thin film: The first step was the electrodeposition of the Cu template by applying -0.5 V for 600 s, the electrolyte was composed of 0.005 M CuSO_4 and 0.1 M K_2SO_4 . The second step was the electro-oxidation of the Cu template by applying 1.2 V for 600 s, where 0.005 M $\text{C}_{16}\text{H}_{36}\text{ClNO}_4$ and 0.00125 M $\text{C}_{21}\text{H}_{15}\text{NO}_6$ were used as the supporting electrolyte and linking agent in a mixture of DMF and deionized water with a volume ratio of 2:1 [34].

Zn-TCA thin film: The first step was the electrodeposition of the Zn template by applying -1.0 V for 800 s, the electrolyte was 0.1 M $\text{Zn}(\text{NO}_3)_2 \cdot 6\text{H}_2\text{O}$ [35]. The second step was the electro-oxidation of the Zn template by applying 1.2 V for 600 s, the electrolyte was the same as that of Cu-TCA.

Co/Cu-TCA thin film: The first step was the electrodeposition of Co/Cu template by applying a constant current of $0.48 \text{ mA} \cdot \text{cm}^{-2}$ for 800 s, the electrolyte was a mixture of 0.12 M $\text{CoCl}_2 \cdot 6\text{H}_2\text{O}$, 0.036 M CuSO_4 , 0.258 M $\text{Na}_3\text{C}_6\text{H}_5\text{O}_7 \cdot 2\text{H}_2\text{O}$ and 0.017 M Na_2SO_4 in deionized water. The pH of the electrolyte was adjusted to 6 by adding 3 M NaOH. The second step was the electro-oxidation of the Co/Cu template by applying 0.8 V for 1000 s, the electrolyte was the same as that of Cu-TCA. The current density evolution, optical transmittance and SEM

images of the Co/Cu-TCA thin film during the electro-oxidation process are shown in Fig. S2, S3. The Co-TCA thin film was also deposited for comparison, the detailed preparation process was presented in the supplementary data.

HKUST-1 and Zn-MOF-74 thin films were deposited by the spin-coating method.

HKUST-1 thin films: 30 mg of the HKUST-1 powder was dispersed into 1 mL of hexane by sonication for 10 min, then the prepared dispersion was spin-coated onto the ITO-coated glass substrate at 800 rpm for 60 s.

Zn-MOF-74 thin films: 30 mg of the Zn-MOF-74 powder was dispersed into 1 mL of deionized water by sonication for 10 min, then the prepared dispersion was spin-coated onto the ITO-coated glass substrate at 1500 rpm for 60 s.

2.3. Characterization and electrochemical measurements

Surface structures of five MOF thin films were observed using a scanning electron microscopy (SEM, SU8020) employing a Zeiss Sigma HD instrument at 10 kV acceleration voltage. Energy-dispersive spectroscopy (EDS) was measured using an Oxford X-Max 150. The cross sections of the films were investigated by SEM with an acceleration voltage of 2 kV. The crystalline structure data were collected using an X-ray diffraction (XRD, Rigaku D/MAX 2500V). The samples were held in a non-reflective holder stage with the scan speed of 5° min^{-1} . The XRD patterns of Cu-TCA, Zn-TCA and Co/Cu-TCA thin films were measured together with the ITO-coated glass substrate, while the HKUST-1 and Zn-MOF-74 powder were used for measurements. Attenuated total reflectance Fourier transform infrared (ATR-FTIR) spectra were taken with an IRTracer-100 FTIR spectrometer equipped with a MIRacle 10 single reflection ATR and a ZnSe detector. Elemental compositions for the surfaces of the Cu-TCA and Co/Cu-TCA thin films were determined by an X-ray

photoelectron spectrometer (XPS, INA-X), which was excited by an Al K_{α} radiation source at a constant power of 100 W (15 kV and 6.67 mA). The samples were cleaned by isopropanol to remove the residue electrolyte and dried under airflow, then cut them into pieces of size $1 \times 0.5 \text{ cm}^2$ for the XPS measurement. The specific surface area was determined using the Brunauer-Emmett-Teller (BET) surface area analyzer (ASAP 2460 3.01). The activation of sample (~140 mg) was performed at 120°C under vacuum for 12 h before measurement. The adsorption and desorption of nitrogen was performed at 298 K. The electrical conductivity was measured using a resistivity tester (ST2253y). Thermogravimetric analyses (TGA) were performed with a heating rate of 10 °C/min from 30 to 800°C in a simulated N₂ atmosphere using a NETZSCH STA 449F3 simultaneous TG-DSC instrument. The ratios of C, H, O and N atoms were recorded with an UNICUBE CHN/O elemental analyzer. The Inductively Coupled Plasma Atomic Emission Spectroscopy (ICP-AES) was determined by Agilent 7700 ICP-MS. The mass of film was weighed by electronic balance (BSA224S) and the data were presented in Table S1.

The electrochemical measurements were carried out in a three-electrode system with a MOF thin films as working electrode, Ag/AgCl as reference electrode, and a platinum wire as counter electrode. The electrolyte was 0.1 M LiClO₄-PC. Cyclic voltammetry (CV) was performed at various scan rates in the selected potential range.

Chronoamperometric (CA) measurements were carried out by switching the potential between 0.8 V and 1.4 V with an interval of 10 s. Electrochemical impedance spectroscopy (EIS) was measured in the frequency range of 0.1 to 500000 Hz with a voltage perturbation of 2 mV. In-situ transmittance of the films was recorded together with the electrochemical measurements in the wavelength of 400-850 nm by an Ocean Optics spectrometer. The quartz vessel was positioned between a tungsten halogen lamp and the detector, and the vessel containing only the electrolyte was employed to obtain the 100% level for transmittance.

3. Results and discussion

3.1. Characterization of the Cu-TCA, Zn-TCA, HKUST-1 and Zn-MOF-74 thin films

Surface structures of the Cu-TCA, Zn-TCA, HKUST-1 and Zn-MOF-74 thin films were shown in Fig. 2a-d, and those of the Cu and Zn templates used were displayed in Fig. S4a, b. All MOF thin films were well-distributed on the surface of the ITO-coated glass substrates and exhibited an irregular cubic structure, an irregular layered structure, an octahedral structure, and loose structure with irregular polycrystalline particles, respectively. XRD was carried out to identify the crystallographic structure of the four MOF thin films and the ITO-coated glass substrates, as shown in (Fig. 2a'-d') and Fig. S4d. All XRD patterns were consistent with the literatures reported, and showed good crystallinity with no traces of other phases or impurity. ATR-FTIR spectroscopy was applied to characterize of the molecular configuration of the thin films. Positions of the absorption peaks of the MOF thin films were quite different from those of their metal center templates (Cu and Zn in Fig. 2a''-c'') or the organic ligand (dobdc⁴⁻ in Fig. 2d''), and provided clear evidence for the presence of the TCA³⁻ ligand in Cu-TCA and Zn-TCA, BTC³⁻ ligand in HKUST-1 and coordination of the hydroxyl group in Zn-MOF-74. XRD and ATR-FTIR data were discussed in detail in the supplementary data. The results indicated successful syntheses of the Cu-TCA, Zn-TCA, HKUST-1 and Zn-MOF-74 thin films.

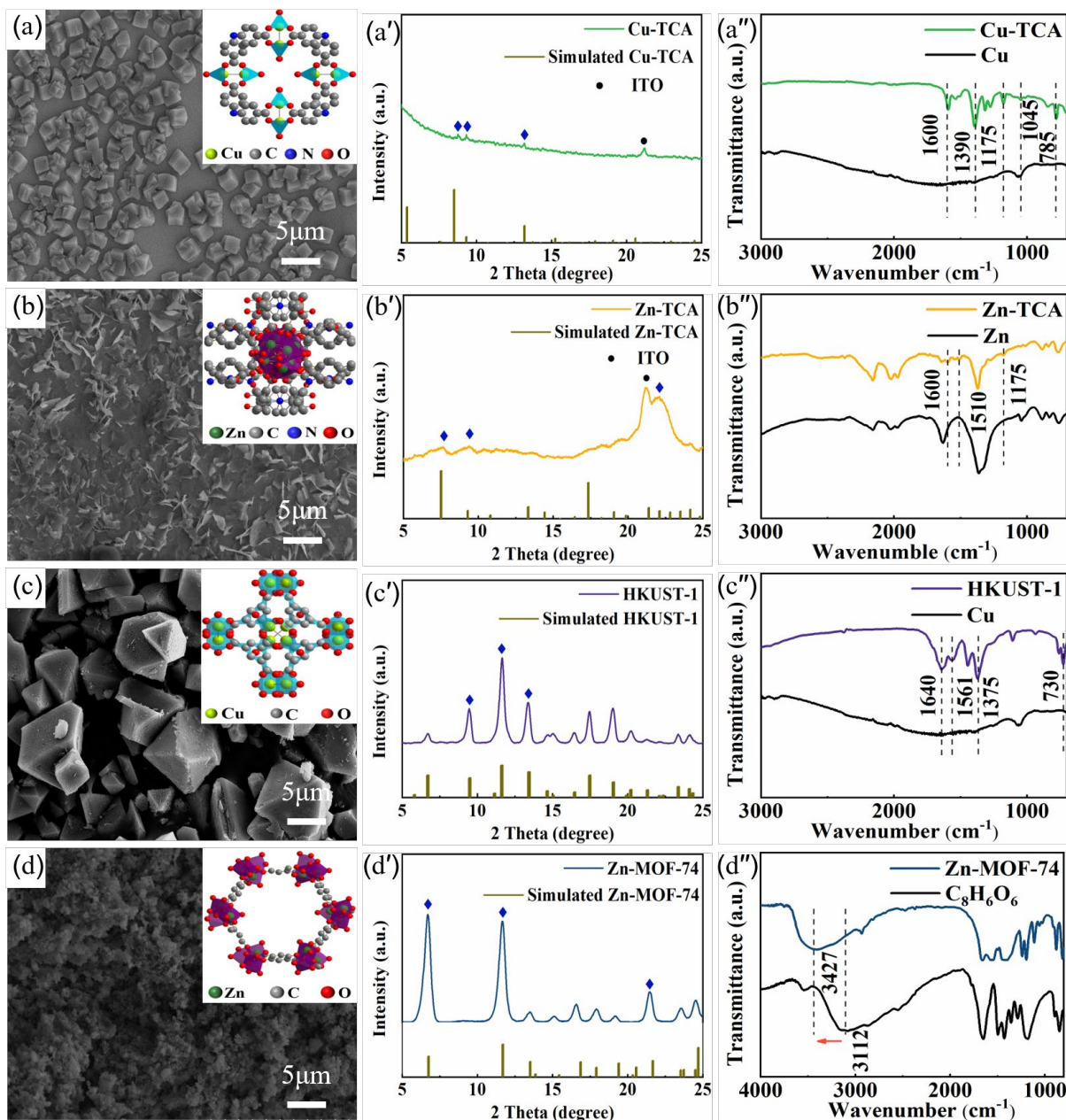


Fig. 2. SEM images of (a) Cu-TCA, (b) Zn-TCA, (c) HKUST-1, and (d) Zn-MOF-74 thin films. XRD patterns of (a') the Cu-TCA thin film, (b') the Zn-TCA thin film, (c') HKUST-1 powder, and (d') Zn-MOF-74 powder. Dots mark the positions of the reflections due to ITO. ATR-FTIR spectra of (a'') Cu-TCA, (b'') Zn-TCA, (c'') HKUST-1, and (d'') Zn-MOF-74 thin films and their metal center templates (Cu and Zn in Fig. 2a''- c'') or the organic ligand (dobdc⁴⁻ in Fig. 2d'').

3.2. EC performance of the Cu-TCA, Zn-TCA, HKUST-1 and Zn-MOF-74 thin films

The EC performance of the Cu-TCA, Zn-TCA, HKUST-1 and Zn-MOF-74 thin films ($1 \times 1 \text{ cm}^2$) was investigated by CV cycling at a scan rate of $50 \text{ mV} \cdot \text{s}^{-1}$ in the electrolyte of $0.1 \text{ M LiClO}_4\text{-PC}$ (Fig. 3). The potential range selected and reaction equations for each kind of films were shown in Table S2. As shown in Fig. 3a, within the cycling potential range, the maximum current densities of the Zn-TCA, HKUST-1 and Zn-MOF-74 thin films were similar and quite small ($\sim 0.15 \text{ mA} \cdot \text{cm}^{-2}$). In addition, HKUST-1 and Zn-MOF-74 thin films presented no obvious oxidation peaks, indicating the irreversibility of their electrochemical processes. In contrast, Cu-TCA and Zn-TCA exhibited much better reversibility with a pair of redox peaks. Cu-TCA showed much larger area enclosed by the CV curve with increased peak current density, as evidenced by the comparison with the other three thin films, indicating more efficient ClO_4^- and electrons transition between the Cu-TCA thin film and the electrolyte.

As discussed above, electrochromism is directly connected with charge intercalation/deintercalation, and can be mirrored by optical modulation. In-situ transmittance spectra of the Cu-TCA, Zn-TCA, HKUST-1 and Zn-MOF-74 thin films were studied in the $400\text{--}850 \text{ nm}$ wavelength range in their initial (as-prepared) states, colored and bleached states during CV cycling. The colored and bleached states were recorded at the highest/lowest potential for Cu-TCA and Zn-TCA thin films because they are anodically coloring materials, and at lowest/highest potential for the HKUST-1 thin film due to its cathodic coloration nature. As shown in Fig. 3b-e, Cu-TCA exhibited the best EC optical modulation among the four MOF thin films. The as-prepared Cu-TCA thin film was light yellow, it can be switched between light yellow and blue during CV cycling in the potential range of 0.8 V to 1.4 V due to the reversible change between N^0 and N^+ in the TCA^{3-} ligand. The largest transmittance modulation was found to be 48% at the wavelength of 705 nm (Fig. 3b). However, for the Zn-TCA thin film with the same organic ligand as Cu-TCA, it can only be switched between light

gray and dark gray, and its largest transmittance modulation was only 12% at the wavelength of 705 nm (Fig. 3c), which was much smaller than that of the Cu-TCA thin film. It is noted that within the potential ranges selected for Cu-TCA and Zn-TCA thin films, there was only one pair of redox peaks in their CV curves. The oxidation peak located at ~ 1.4 V corresponds to the oxidation of N^0 to N^+ in the TCA^{3-} ligand, and the reduction peak located at ~ 1.1 V is due to the reduction of N^+ to N^0 in the TCA^{3-} ligand [29]. Thus, the electrochromism of Cu-TCA and Zn-TCA resulted from the reversible oxidation and reduction of the TCA^{3-} ligand. The reason for the larger transmittance modulation of Cu-TCA can be assigned to the reduced band gap of Cu-TCA by its redox-active metal center Cu, leading to easier electronic transition and the increased redox ability [36] (Fig. 3f, Fig. S5, as discussed in detail in the supplementary data). The transmittance modulation of the HKUST-1 thin film (Fig. 3d) was even smaller, its electrochromism was due to the valence change of the metal center Cu [37] between Cu^{2+} and Cu^+ with the reduction peak at -1.7 V. And the transmittance of the Zn-MOF-74 thin film did not change during CV cycling since neither of the metal center Zn and the $dobdc^{4-}$ ligand had redox activity. Photos of the films in their initial, colored and bleached states were shown in Table S2.

As a result, we conclude that both metal centers and organic ligands are significant for the EC performance of MOFs. If MOF thin films are composed of redox-inactive organic ligands and redox-inactive metal centers, they cannot exhibit EC performance, such as Zn-MOF-74. When MOFs contain redox-active organic ligands or redox-active metal centers, their optical properties can be varied reversibly, such as Cu-TCA, Zn-TCA and HKUST-1 discussed above. Cu-TCA and Zn-TCA have the same redox-active organic ligand but different metal centers, the redox-active metal center Cu leads to a smaller band gap of Cu-TCA and easier electron transition, resulting in better EC performance. The difference in the EC performance of Cu-TCA and HKUST-1 was related to the different organic ligands, HKUST-1 exhibited low redox activity for its redox-inactive organic.

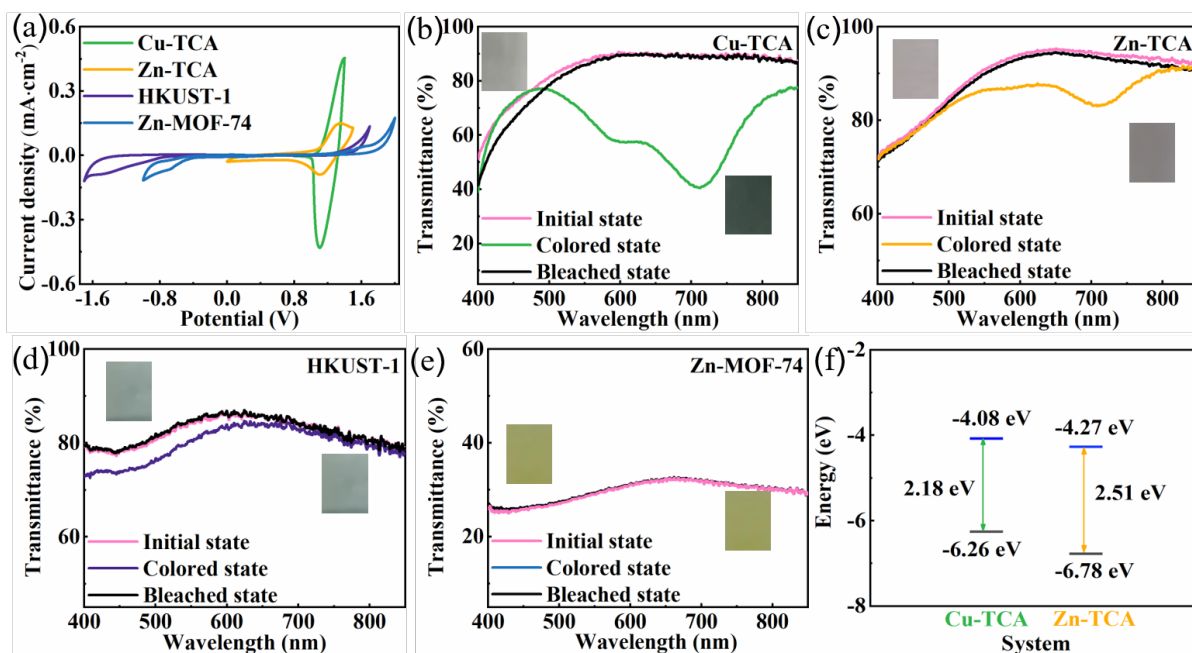


Fig. 3. (a) CV curves of the Cu-TCA, Zn-TCA, HKUST-1, and Zn-MOF-74 thin films at 50 $\text{mV}\cdot\text{s}^{-1}$ in 0.1 M $\text{LiClO}_4\text{-PC}$. Transmittance modulation and corresponding photos of the (b) Cu-TCA, (c) Zn-TCA, (d) HKUST-1, and (e) Zn-MOF-74 thin films during CV cycling, (f) comparison of the band gaps of Cu-TCA and Zn-TCA.

3.3. Characterization of the Co/Cu-TCA thin film

After a careful selection of proper metal centers and organic ligands, we attempted to dope another redox-active metal Co^{2+} into Cu-TCA to form the Co/Cu-TCA thin film, since doping can increase the specific surface area and pore volume and facilitate the migration of ions and electrons. The Co^{2+} ion was selected due to the same coordination number as Cu^{2+} , and it is easily to be introduced by electrodeposition, see details in the Experimental section. Fig. 4a shows the surface SEM image of the Co/Cu-TCA thin film, morphology of the Co/Cu template used was displayed in Fig. S4c. Co/Cu-TCA exhibited a rough surface with irregular cubes well-distributed on the ITO-coated glass substrate. It is noticed that the shape and size of the Cu-TCA became more regular and uniform after doping Co^{2+} . In addition, the thicknesses of both Cu-TCA and Co/Cu-TCA thin films were ~ 400 nm, as displayed in Fig. S6. Compared with the simulated XRD pattern of the Cu-TCA thin film, the peak assigned to

the (112) plane at $2\theta = 9.3^\circ$ shifted to lower degree of 9.1° after Co^{2+} doping (Fig. 4b). According to the Bragg formula $2d \cdot \sin\theta = \lambda$ (d represents interplanar spacing; θ and λ represent angle and diffraction wavelength of the light inside the crystal), the decrement in θ at the (112) plane indicates the increment of the interplanar spacing d due to Co^{2+} doping. This is because the ionic radius of Co^{2+} (0.0745 nm) is larger than that of Cu^{2+} (0.0730 nm), substitution of Co^{2+} for Cu^{2+} leads to the expansion of the Cu-TCA lattice, leading to the increased space between (112) planes. XRD patterns of the Co/Cu-TCA thin films with varied Co concentrations ($\text{Co}/(\text{Cu} + \text{Co}) = 0, 0.1, 0.2$ and 0.3) were shown in Fig. S7.

The ATR-FTIR spectrum of the Co/Cu-TCA thin film was displayed in (Fig. 4c), Co/Cu-TCA maintained the same functional groups except for the increased intensity of peaks within the range of $1000\text{--}1200\text{ cm}^{-1}$ due to the formation of Co-O. To further study the element distribution of Cu-TCA and Co/Cu-TCA thin films, EDS analysis was carried out with a typical top-view SEM image and corresponding C, N, O, Cu and Co maps were taken Fig. S8, Fig. 4d. The element maps show that C and Cu were mainly localized within the inner micro-cubic structure, while N, O and Co were distributed in all areas since Co^{2+} coordinated with O^{2-} in Co/Cu-TCA, indicating that Co^{2+} had been successfully doped into the lattice of the Cu-TCA thin film. Elemental analyses were recorded by elemental analyzer and ICP-AES. Calcd (%) for Co/Cu-TCA: C, 53.85; H, 2.56; N, 2.99; O, 20.5. Found (%): C, 53.82; H, 2.55; N, 3.02; O, 20.2. Determined by ICP-AES, the weight percentages of Cu and Co were 16.1% and 3.8% in Co/Cu-TCA, respectively.

Thermogravimetric analyses for Co/Cu-TCA were carried out to examine the thermal stability (Fig. S9). The first weight loss stage started at $30\text{ }^\circ\text{C}$ and ended at $140\text{ }^\circ\text{C}$, accompanied by about 4.9% weight loss corresponding to the loss of the adsorbed water. The second weight loss of 79.7% occurred at the temperature range of $200\text{--}700\text{ }^\circ\text{C}$, which can be ascribed to the

collapse of the main framework. TGA results show good thermostability of the as-prepared Co/Cu-TCA below 200 °C.

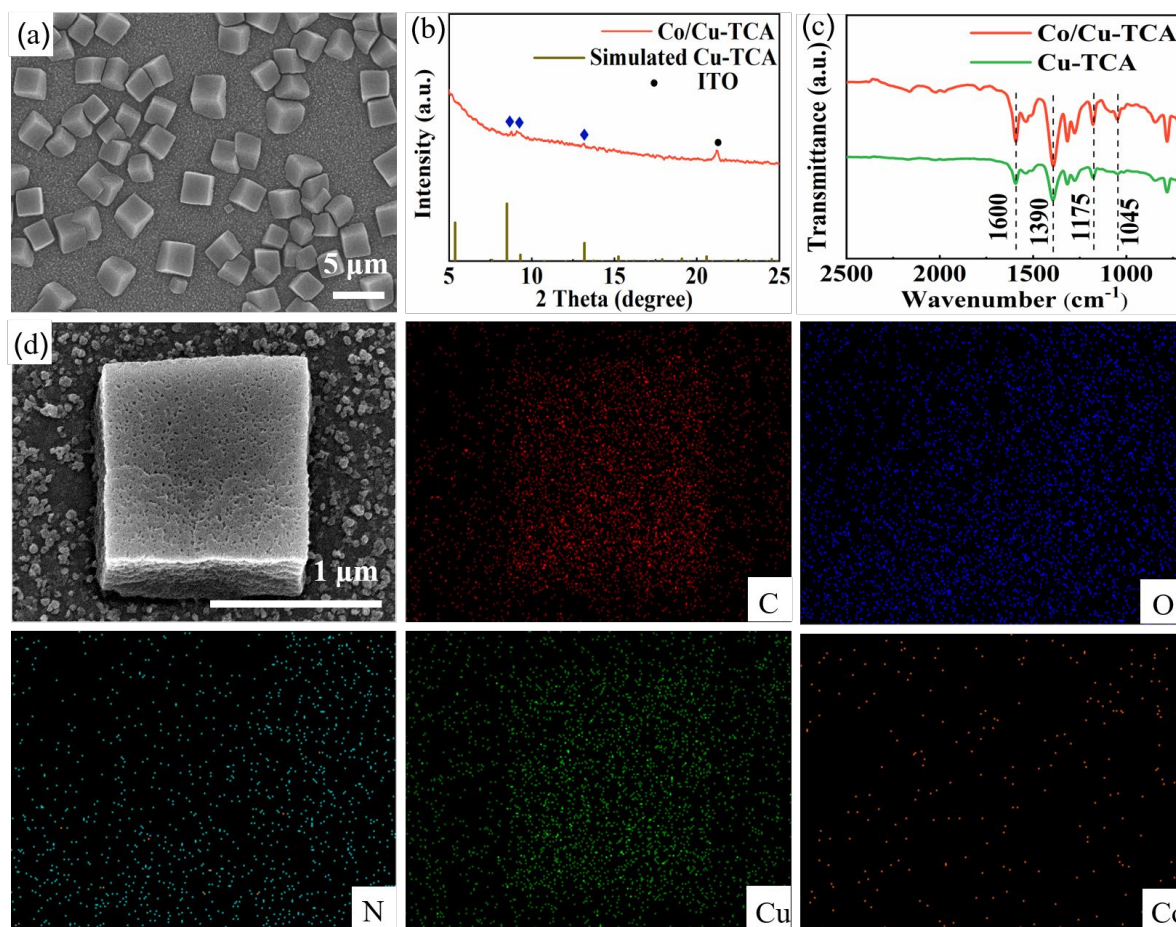
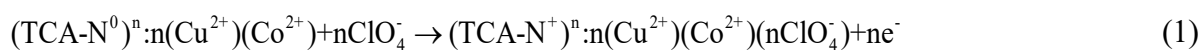


Fig. 4. (a) SEM image of the Co/Cu-TCA thin film, (b) XRD pattern of the Co/Cu-TCA thin film, (c) ATR-FTIR spectra of the Co/Cu-TCA thin film and its Co/Cu template, (d) SEM image and corresponding elemental mapping of C, O, N, Cu and Co for the Co/Cu-TCA thin film.

3.4. Electrochemical properties of the Cu-TCA and Co/Cu-TCA thin films

The electrochemical properties of the Cu-TCA and Co/Cu-TCA thin films were investigated by CV and EIS. The CV curves of the Cu-TCA and Co/Cu-TCA thin films were recorded at various scan rates in the potential range of 0.8 V to 1.4 V, as shown in Fig. 5a, b. CV curves of the Co/Cu-TCA thin films with varied Co concentrations were shown in Fig. S10.

Similar as the CV curve of the Cu-TCA film, only one pair of redox peaks appeared in the CV curve of Co/Cu-TCA, indicating a redox reaction process had occurred. The reduction peaks of the Cu-TCA and Co/Cu-TCA thin films were exhibited in Fig. 5a, b, respectively. For instance, 1.20 V and 1.17 V for Cu-TCA and Co/Cu-TCA samples at a scan rate of $10 \text{ mV}\cdot\text{s}^{-1}$. They shifted to lower potentials (i.e. the scan direction) with an increase in the scan rate, e.g. 1.18 V and 1.15 V for Cu-TCA and Co/Cu-TCA samples at a scan rate of $20 \text{ mV}\cdot\text{s}^{-1}$, which is an indication of the quasi-reversible system. As for the oxidation peaks, Cu-TCA showed obvious oxidation peaks at slow scan rates of $10 \text{ mV}\cdot\text{s}^{-1}$ and $20 \text{ mV}\cdot\text{s}^{-1}$, appearing at 1.30 V and 1.33 V, respectively, as shown in Fig. 5a. They moved to higher potentials with increased scan rates, which exceeded the potential range we applied. Co^{2+} doping improved the cyclic charge exchange with larger current densities, as displayed in Fig. 5b. The oxidation peak only appeared at the slowest scan rate of $10 \text{ mV}\cdot\text{s}^{-1}$. The same as that of the Cu-TCA thin film, it shifted to potentials higher than 1.4 V and thus did not appear in Fig. 5b. During scan from 0.8 V to 1.4 V, the current gradually increased as a result of the intercalation of ClO_4^- into Co/Cu-TCA, and the film became navy blue in color. In contrast, during scan in the opposite direction, the Co/Cu-TCA thin film bleached to light yellow with the deintercalation of ClO_4^- . The intercalation/deintercalation of ClO_4^- resulted in the valence change of nitrogen from N^0 to N^{+1} in the TCA^{3-} ligands. Therefore, the electrochemical process of the Co/Cu-TCA thin film can be expressed as



In addition, larger current densities were observed in the Co/Cu-TCA thin film compared with the Cu-TCA thin film at the same scan rate, leading to an improved cyclic charge exchange. The specific capacities were calculated from the CV curves in Fig. 3a and 5c (both of the scan rates are $50 \text{ mV}\cdot\text{s}^{-1}$) according to Equation (2) [38]

$$C = \frac{1}{2\nu\Delta V} \int IdV \quad (2)$$

where C , I , V , ν , and ΔV represent areal specific capacitance, instantaneous current density, instantaneous potential, scan rate, and potential difference. The initial specific capacities of Cu-TCA and Co/Cu-TCA thin films were 2.97, and 3.56 $\text{mF}\cdot\text{cm}^{-2}$, respectively. The results provide clear evidence that the Co/Cu-TCA thin film has enhanced intrinsic electrochemical activity, which is mainly contributed from larger specific surface area and pore volume (Fig. S12), resulting in more ClO_4^- intercalation/deintercalation in the electrochemical process.

To further study the effect of cobalt incorporation on the electrochemical performance of the Cu-TCA thin film, the ClO_4^- diffusion coefficients of the Cu-TCA and Co/Cu-TCA thin films were calculated using the Randles–Sevcik formula [39]

$$I_p = 0.4463ZFA \left(\frac{ZF}{RT} \right)^{\frac{1}{2}} C_0 D^{\frac{1}{2}} \nu^{\frac{1}{2}} \quad (3)$$

where I_p is the peak current, Z is the number of transferred electrons involved in the redox process (Z is taken as 1 in the case of the Cu-TCA and Co/Cu-TCA thin films), c is the concentration of ClO_4^- in the electrolyte, A is the effective surface area of the electrode. Fig. 5d shows that the current densities of the reduction peaks derived from Fig. 5a, b have a good linear relationship with the square root of the scan rate $\nu^{1/2}$, demonstrating that intercalation of ClO_4^- was controlled by ion diffusion from the electrolyte to the surface of the Cu-TCA and Co/Cu-TCA thin films. It is noted that the calculated ClO_4^- diffusion coefficients of the Cu-TCA and Co/Cu-TCA thin films from Fig. 5d were $6.93 \times 10^{-9} \text{ cm}^2 \cdot \text{s}^{-1}$ and $3.81 \times 10^{-9} \text{ cm}^2 \cdot \text{s}^{-1}$, respectively, which may be attributed to the better conductivity of the Cu-TCA film ($200 \text{ S}\cdot\text{m}^{-1}$) than the Co/Cu-TCA thin film ($177 \text{ S}\cdot\text{m}^{-1}$). The ClO_4^- diffusion coefficients of both films are lower than other materials (Table S4), which is due to the poor conductivity of the TCA^{3-} . This can be further illustrated by the Nyquist plots of the Cu-TCA and Co/Cu-TCA

thin films in Fig. 5e. The impedance curves showed an incomplete semicircle with a tail on its right side. The circuit model used in Fig. 5f fitted well with the experimental EIS data in Fig. 5e. R_s is the high frequency resistance representing the electrolyte, R_{ct} and $CPE1$ represent to the charge-transfer resistance and the double-layer capacitance at the interface of the thin film and the electrolyte [40]. R_f and $CPE2$ represent the resistance and the double-layer capacitance at the interface of the thin film and the ITO layer, respectively. The Cu-TCA thin film exhibited a much lower R_{ct} value of 182.6 Ω than that of the Co/Cu-TCA thin film (192.6 Ω), indicating a slower ion diffusion resistance of the Co/Cu-TCA thin film.

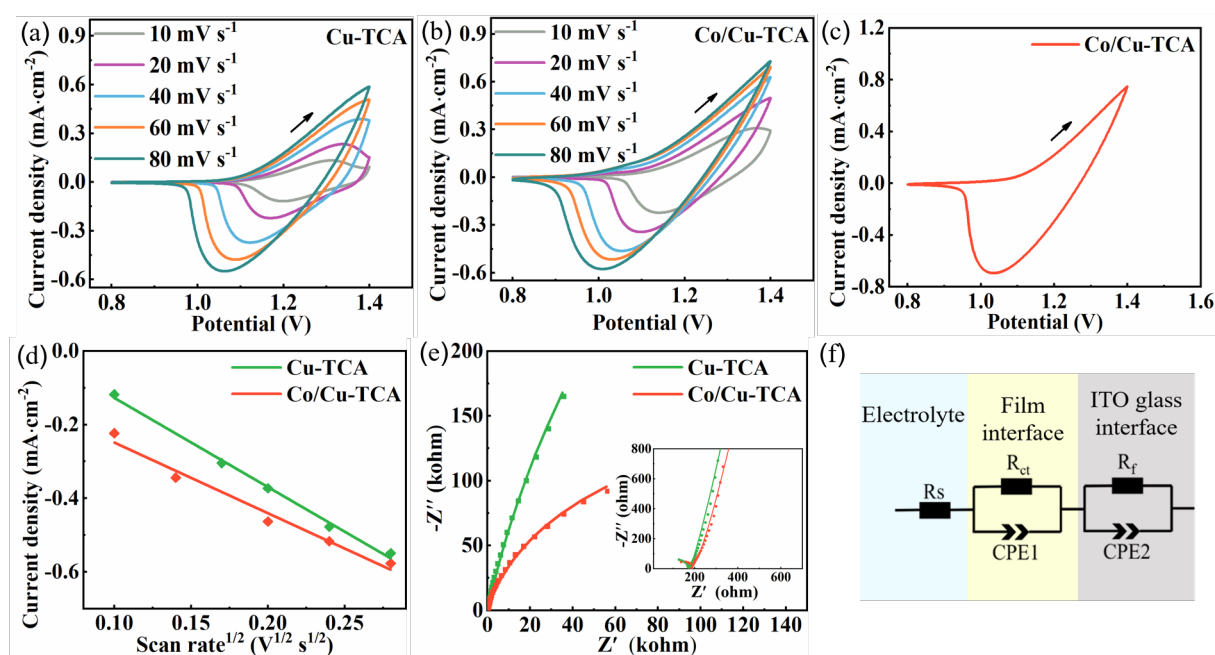


Fig. 5. CV curves of the (a) Cu-TCA and (b) Co/Cu-TCA thin films at various scan rates, (c) CV curve of the Co/Cu-TCA thin film at $50 \text{ mV} \cdot \text{s}^{-1}$, (d) linear fit of the peak current I_p and the square root of the scan rate $v^{1/2}$ of the Cu-TCA and Co/Cu-TCA thin films, (e) Nyquist plots of the Cu-TCA and Co/Cu-TCA thin films, (f) the circuit model used to fit the Nyquist plots in Fig. 5e.

3.5. EC performance of the Cu-TCA and Co/Cu-TCA thin films

A spectro-electrochemical method was used to evaluate the optical properties of the Cu-TCA and Co/Cu-TCA thin films in the potential range of 0.8 V to 1.4 V. Compared with Cu-TCA, optical modulation of the Co/Cu-TCA thin film was larger at 550 nm (the most sensitive wavelength for human's eyes) and 705 nm (the wavelength where the largest optical modulation located), which were 46% and 70%, respectively, with more transparency in the bleached state and deeper blue in the colored state (Fig. 6a), indicating that the addition of Co^{2+} can increase the optical modulation of the Cu-TCA thin film. Co^{2+} doping can increase the specific surface area and pore volume of Cu-TCA (Fig. S11a, b), facilitating ClO_4^- migration and electrons intercalation/deintercalation. Transmittance modulation of Co/Cu-TCA thin films with other Co concentrations was also measured and shown in Fig. S11.

The coloration efficiency (CE) is an important standard for evaluating the EC performance. CE is defined as the change in optical density (ΔOD) at a specific wavelength per unit injection charge density (ΔQ) in coloring process, and can be calculated by Equation (4) [41]

$$CE = \frac{\Delta OD}{\Delta Q} = \frac{\log\left(\frac{T_b}{T_c}\right)}{\Delta Q} \quad (4)$$

where T_c and T_b denote the transmittance of the colored state and the bleached state, respectively. It can be seen from Fig. 6b that after Co doping, the CE was significantly increased to $337 \text{ cm}^2 \cdot \text{C}^{-1}$, much larger than that of the Cu-TCA thin film ($197 \text{ cm}^2 \cdot \text{C}^{-1}$) and other MOFs (Table S4). The enhanced coloration efficiency of the Co/Cu-TCA thin film resulted from more ClO_4^- ions participated in the electrochemical process due to its larger specific surface area and pore volume. We also tested the switching speed of the Cu-TCA and Co/Cu-TCA thin films. The transmittance spectra were obtained by CA by applying a pulsed potential of 0.8 V and 1.4 V for 10 s each at 705 nm (Fig. 6c). Switching time is defined as the time required to reach 90% change between the bleached state and the colored state. Due

to smaller ClO_4^- diffusion coefficient of the Co/Cu-TCA thin film, it exhibited a longer switching time for the coloration (3.3 s) and bleaching (6.0 s) processes compared with that of the Cu-TCA thin film (2.2 s and 4.2 s, respectively), as shown in Fig. 6d. Meanwhile, durability of the Cu-TCA and Co/Cu-TCA thin films was examined during 500 CA cycles. Optical contrast of both films can be improved by increasing the potential range applied, but the durability would be sacrificed at the same time (Fig. S13, S14). Especially, when the potential range of 0.8 V to 1.5 V was applied, the thin films showed more rapid degradation at first and then slowly fell off from the ITO-coated glass substrates, resulting in severe degradation of the current density and optical modulation. Therefore, we studied the durability of the Cu-TCA and Co/Cu-TCA thin films by applying a pulsed potential of 0.8 V and 1.4 V for 10 s each at 705 nm. During 500 CA cycles, the initial optical modulation of the Co/Cu-TCA thin film was 70%, much larger than that of the Cu-TCA thin film (48%). However, it is apparent that faster degradation occurred for the Co/Cu-TCA thin film, both for its current density (Fig. 6e) and optical modulation (Fig. 6f). Transmittance modulation and charge capacity degradation of the Cu-TCA and Co/Cu-TCA thin films were shown in Fig. S15.

After 500 CA cycles, the optical contrast of two films was almost the same. Besides, after 500 CV cycles, the Cu-TCA and Co/Cu-TCA thin films retained their initial shape with some pores appearing on the cubes (Fig. S16). Compared with Cu-TCA, the slower ClO_4^- diffusion coefficients of Co/Cu-TCA impeded the migration of ClO_4^- , resulting in more ion trap and less active sites for the redox reaction during the EC process [42-43].

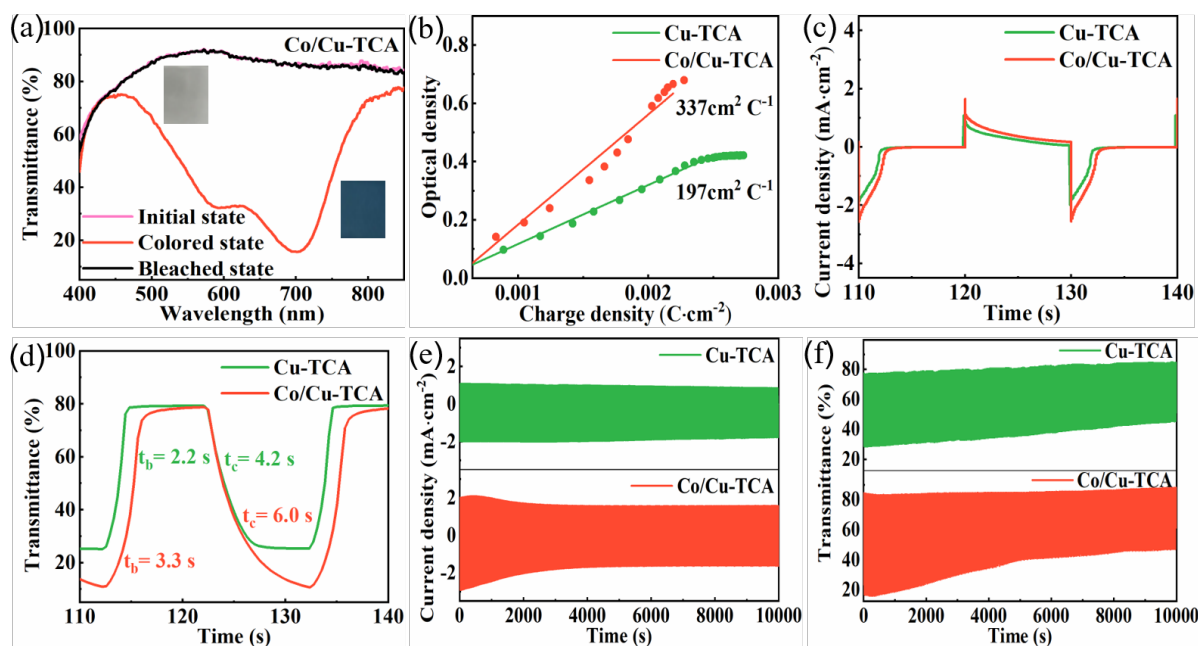


Fig. 6. (a) Transmittance modulation and corresponding photos of the Co/Cu-TCA thin film during CV cycling in the potential range of 0.8 V to 1.4 V, (b) coloration efficiencies of the Cu-TCA and Co/Cu-TCA thin films, (c) CA curves of the Cu-TCA and Co/Cu-TCA thin films, (d) switching time of the Cu-TCA and Co/Cu-TCA thin films, (e, f) electrochemical and optical durability of the Cu-TCA and Co/Cu-TCA thin films tested during 500 CA cycles by applying a pulsed potential of 0.8 V and 1.4 V for 10 s each at 705 nm.

To shed light on the effect of Co doping on the composition and structure of Cu-TCA, XPS was used to examine elemental compositions and chemical states for the surface of both Cu-TCA and Co/Cu-TCA thin films. The samples in the initial state, colored state and bleached state were examined, and the data of the survey scans were given in Table S4. Features due to C, N, O, Cu were shown in both Cu-TCA and Co/Cu-TCA, and Co was successfully doped in the Co/Cu-TCA thin film with the atomic fraction of 20% (Fig. 7a, b), which were consistent with results displayed in the element mappings and ICP-AES. In order to further explore the coordination structure of each element, high-resolution XPS spectra pertaining to individual elements were fitted with deconvolution and Gaussian curves. High-resolution spectra of C 1s for Cu-TCA and Co/Cu-TCA can be deconvoluted into peaks at 284.8, 285.6 and 288.5 eV, corresponding to C-C, C-N and C=O signals [44, 45] (Fig. 7a', b'). N⁺ and N⁰ in

triphenylamine was observed in the N 1s spectra in the initial state locating at 401 eV and 400 eV [46, 47], respectively (Fig. 7a'', b''). N⁺ appeared in the organic ligand TCA³⁻ in initial state due to the partial oxidation in air [47]. The deconvoluted peaks of O 1s at 533.5 eV, 532.1 eV, 531.5 eV and 531.1 eV can be attributed to O-H, C=O, Cu-O and Co-O [48-50] (Fig. S17a and S18a). The Cu 2p XPS spectra of Cu-TCA exhibited two peaks at 954.4 eV and 934.6 eV [51] (Fig. S17b), corresponding to the Cu 2p_{1/2} and Cu2p_{3/2}, respectively. However, it displayed two sets of peaks assigned to Cu⁺ (932.5 and 952.33 eV) and Cu²⁺ (934.6 eV, 954.3 eV) [52] for Co/Cu-TCA due to the decreased valence of Cu caused by Co²⁺ doping (Fig. S18b). Fig S18c shows the Co 2p spectra, the binding energy of Co²⁺ was 781.3 eV, with one shake-up satellite peak at 803.5 eV [53], confirming the incorporation of Co²⁺ in the Cu-TCA. The zoomed-in XPS peaks of Cu 2p and Co 2p for the Cu-TCA and Co/Cu-TCA thin films in the initial, colored, and bleached states were shown in Fig. S19. Data derived from the high-resolution spectra of C 1s, N 1s, and O 1s, Cu2p and Co 2p for the Cu-TCA and Co/Cu-TCA thin films were exhibited in Table S6 and S7, respectively. It is specially noted that the atomic ratio of C-N, N⁰ and N⁺ varied during the EC process with the transport of ClO₄⁻. During the coloring process, ClO₄⁻ intercalated into the Cu-TCA and Co/Cu-TCA thin films to absorb on the nitrogen atoms, resulting in the increased ratio of N⁺ and decreased ratio of C-N and N⁰. In contrast, during the bleaching process, ClO₄⁻ ions migrated out of the thin films, leading to the decreased ratio of N⁺. The peak position and atomic ratio of Cu⁺, Cu²⁺ and Co²⁺ changed little during the EC process, indicating the EC redox reaction of the films was not dominated by the metal centers. Clearly, the valence change of N in TCA³⁻ ligands by ClO₄⁻ intercalation/deintercalation leads to transmittance modulation of the Cu-TCA and Co/Cu-TCA thin films (Fig. 7c). Moreover, the incorporation of Co²⁺ can increase the specific surface area and pore volume of Cu-TCA facilitate ClO₄⁻ intercalation/deintercalation, as evidenced by the increased atomic ratio change of N⁰ and N⁺

(21% for Cu-TCA and 35% for Co/Cu-TCA), resulting in the enhanced transmittance modulation and coloration efficiency.

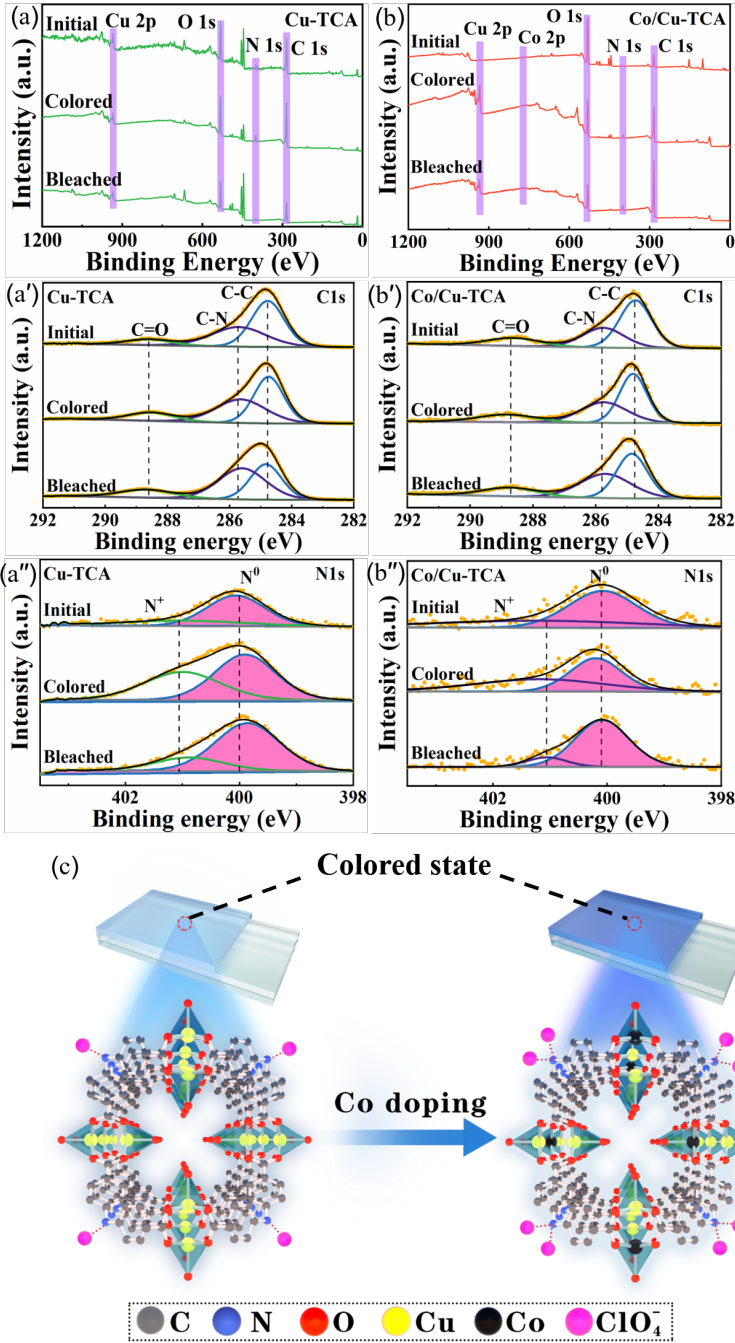


Fig. 7. (a, b) XPS survey scans of the Cu-TCA and Co/Cu-TCA thin films in the initial, colored, and bleached stated. High-resolution XPS spectra of (a', b') C 1s and (a'', b'') N 1s for the Cu-TCA and Co/Cu-TCA thin films in the initial, colored, and bleached stated, (c) Schematic showing the possible EC mechanism of the of Cu-TCA and Co/Cu-TCA thin films.

4. Conclusions

In summary, Cu-TCA, Zn-TCA, HKUST-1, Zn-MOF-74 and Co/Cu-TCA thin films containing different redox-active/inactive metal centers and organic ligands were successfully prepared using electrodeposition and spin-coating methods under mild conditions, as verified by XRD, ATR-FTIR, EDS and XPS. Results show that EC properties of MOFs were determined by the redox-active metal center and organic ligand, and the latter one dominated. Among the first four MOFs thin films, Cu-TCA with the redox-active metal center and organic ligand exhibited the best EC performance with transmittance modulation of 50% at the wavelength of 705 nm. Co²⁺ doping into Cu-TCA can increase the specific surface area and pore volume, as revealed by the BET data and the increased atomic ratio change of N⁰ and N⁺ from XPS, facilitating intercalation/deintercalation of ions and electrons. As a result, Co/Cu-TCA thin film exhibited quite high optical contrast (70% at 705 nm) and coloration efficiency (337 cm²·C⁻¹). Our results are applicable also to other redox-active processes of MOFs, such as in batteries and supercapacitors.

Acknowledgments

The authors are grateful for financial support from the National Natural Science Foundation of China (No. 52002087), the Natural Science Foundation of Guangxi Province (No. 2020GXNSFBA297002), the Chinese Central Government Guided Local Science and Technology Development Project (No. Guike AD20238064), the Dean Project of Guangxi Key Laboratory of Petrochemical Resource Processing and Process Intensification Technology (No. 2021Z016) and Special Funding for "Guangxi Bagui Scholars". Dr. Junxin Wang acknowledges financial support from European Union's Horizon 2020 research and innovation programme Marie Skłodowska-Curie Actions under grant agreement number 892131-PECTRA-H2020-MSCA-IF-2019.

References

- [1] G. A. Niklasson, C. G. Granqvist, Electrochromics for smart windows: thin films of tungsten oxide and nickel oxide, and devices based on these, *J. Mater. Chem.* 172 (2007) 127-156. <https://doi.org/10.1039/b612174h>
- [2] R. J. Mortimer, A. L. Dyer, J. R. Reynolds, Electrochromic organic and polymeric materials for display applications, *Displays* 271 (2006) 2-18. <https://doi.org/10.1016/j.displa.2005.03.003>
- [3] J. Lin, M. Lai, L. Dou, C. S. Kley, H. Chen, F. Peng, J. Sun, D. Lu, S. A. Hawks, C. Xie, F. Cui, A. P. Alivisatos, D. T. Limmer, P. Yang, Thermochromic halide perovskite solar cells, *Nat. Mater.* 173 (2018) 261-267. <https://doi.org/10.1038/s41563-017-0006-0>
- [4] M. Devillard, N. Nour Eddine, M. Cordier, G. Alcaraz, Dithienylethene-based photochromic siloles: A straightforward and divergent synthetic strategy, *Angew. Chem. Int. Edit.* 6022 (2021) 12356-12359. <https://doi.org/10.1002/anie.202102540>
- [5] W. Qi, G. Gao, G. Wu, H. Wang, Flexible gasochromic films with favorable high temperature resistance and energy efficiency, *Sol. Energy Mater. Sol. Cells* 195 (2019) 63-70. <https://doi.org/10.1016/j.solmat.2019.01.049>
- [6] R. Baetens, B. P. Jelle, A. Gustavsen, Properties, requirements and possibilities of smart windows for dynamic daylight and solar energy control in buildings: A state-of-the-art review, *Sol. Energy Mater. Sol. Cells* 942 (2010) 87-105. <https://doi.org/10.1016/j.solmat.2009.08.021>
- [7] D. Zhang, J. Wang, Z. Tong, H. Ji, H. Y. Qu, Bioinspired dynamically switchable PANI/PS-b-P₂VP thin films for multicolored electrochromic displays with long-term durability, *Adv. Funct. Mater.* 3145 (2021) 2106577. <https://doi.org/10.1002/adfm.202106577>
- [8] Z. Xie, Q. Liu, Q. Zhang, B. Lu, J. Zhai, X. Diao, Fast-switching quasi-solid state electrochromic full device based on mesoporous WO₃ and NiO thin films, *Sol. Energy Mater. Sol. Cells* 200 (2019) 110017. <https://doi.org/10.1016/j.solmat.2019.110017>
- [9] S. M. Wang, Y. Wang, T. Wang, Z. Han, C. Cho, E. Kim, Charge-balancing redox mediators for high color contrast electrochromism on polyoxometalates, *Adv. Mater. Technol.* 510 (2020) 000326. <https://doi.org/10.1002/admt.202000326>
- [10] S. M. Wang, Y. Kim, B. Kim, M. Han, E. Kim, Ultrathin polyoxometalate coating as the redox shuttle for acid-free electrochromic polymer capacitive windows, *Adv. Funct. Mater.* 2918 (2019) 1806590. <https://doi.org/10.1002/adfm.201806590>

- [11] J. Wang, L. Zhang, L. Yu, Z. Jiao, H. Xie, X. W. Lou, X. W. Sun, A bi-functional device for self-powered electrochromic window and self-rechargeable transparent battery applications, *Nat. Commun.* 5 (2014) 4921. <https://doi.org/10.1038/ncomms5921>
- [12] H. Ling, J. Wu, F. Su, Y. Tian, Y. J. Liu, Automatic light-adjusting electrochromic device powered by perovskite solar cell, *Nat. Commun.* 121 (2021) 1010. <https://doi.org/10.1038/s41467-021-21086-7>
- [13] B. Yang, D. Ma, E. Zheng, J. Wang, A self-rechargeable electrochromic battery based on electrodeposited polypyrrole film, *Sol. Energy Mater. Sol. Cells* 192 (2019) 1-7. <https://doi.org/10.1016/j.solmat.2018.12.011>
- [14] L. Shen, J. Zheng, C. Xu, Enhanced electrochromic switches and tunable green fluorescence based on terbium ion doped WO₃ films, *Nanoscale* 1147 (2019) 23049-23057. <https://doi.org/10.1039/c9nr06125h>
- [15] W. Wang, X. Wang, X. Xia, Z. Yao, Y. Zhong, J. Tu, Enhanced electrochromic and energy storage performance in mesoporous WO₃ film and its application in a bi-functional smart window, *Nanoscale* 1017 (2018) 8162-8169. <https://doi.org/10.1039/c8nr00790j>
- [16] S. Heo, A. Agrawal, D. J. Milliron, Wide dynamic range in tunable electrochromic bragg stacks from doped semiconductor nanocrystals, *Adv. Funct. Mater.* 2937 (2019) 1904555. <https://doi.org/10.1002/adfm.201904555>
- [17] H. Liang, R. Li, C. Li, C. Hou, Y. Li, Q. Zhang, H. Wang, Regulation of carbon content in MOF-derived hierarchical-porous NiO@C films for high-performance electrochromism, *Mater. Horizons* 63 (2019) 571-579. <https://doi.org/10.1039/C8MH01091A>
- [18] B. A. Johnson, A. Bhunia, H. Fei, S. M. Cohen, S. Ott, Development of a UiO-type thin film electrocatalysis platform with redox-active linkers, *J. Am. Chem. Soc.* 1408 (2018) 2985-2994. <https://doi.org/10.1021/jacs.7b13077>
- [19] Y. Zhou, L. Han, Recent advances in naphthalenediimide-based metal-organic frameworks: Structures and applications, *Coord. Chem. Rev.* 430 (2021) 213665. <https://doi.org/10.1016/j.ccr.2020.213665>
- [20] Y. Cui, B. Li, H. He, W. Zhou, B. Chen, G. Qian, Metal-organic frameworks as platforms for functional materials, *Accounts Chem. Res.* 493 (2016) 483-493. <https://doi.org/10.1021/acs.accounts.5b00530>
- [21] C. Hua, P. W. Doheny, B. Ding, B. Chan, M. Yu, C. J. Kepert, D. M. D'Alessandro, Through-space intervalence charge transfer as a mechanism for charge delocalization in metal-organic frameworks, *J. Am. Chem. Soc.* 14021 (2018) 6622-6630. <https://doi.org/10.1021/jacs.8b02638>

- [22] R. Li, K. Li, G. Wang, L. Li, Q. Zhang, J. Yan, Y. Chen, Q. Zhang, C. Hou, Y. Li, H. Wang, Ion-transport design for high-performance Na⁺-based electrochromics, *ACS nano*. 12 (2018) 3759-3768. <https://doi.org/10.1021/acsnano.8b00974>
- [23] H. Wang, F. Yin, N. Liu, H. Yu, T. Fan, B. Chen, Engineering mesopores and unsaturated coordination in metal-organic frameworks for enhanced oxygen reduction and oxygen evolution activity and Li-Air battery capacity, *ACS Sustain. Chem. Eng.* 912 (2021) 4509-4519. <https://doi.org/10.1021/acssuschemeng.0c08811>
- [24] A. M. Ebrahim, T. J. Bandosz, Ce(III) doped Zr-based MOFs as excellent NO₂ adsorbents at ambient conditions, *ACS Appl. Mater. Interfaces* 521 (2013) 10565-10573. <https://doi.org/10.1021/am402305u>
- [25] S. T. Meek, J. A. Greathouse, M. D. Allendorf, Metal-organic frameworks: a rapidly growing class of versatile nanoporous materials, *Adv. Mater.* 232 (2011) 249-267. <https://doi.org/10.1002/adma.201002854>
- [26] H. Furukawa, K. E. Cordova, M. O'Keeffe, O. M. Yaghi, The chemistry and applications of metal-organic frameworks, *Science* 3416149 (2013) 1230444. <http://dx.doi.org/10.1126/science.1230444>
- [27] J. J. Zhou, W. Ji, L. Xu, Y. Yang, W. Wang, H. Ding, X. Xu, W. Wang, P. Zhang, Z. Hua, L. Chen, Controllable transformation of CoNi-MOF-74 on Ni foam into hierarchical-porous Co(OH)₂/Ni(OH)₂ micro-rods with ultra-high specific surface area for energy storage, *Chem. Eng. J.* 428 (2022) 132123. <https://doi.org/10.1016/j.cej.2021.132123>
- [28] P. Wu, J. Wang, Y. Li, C. He, Z. Xie, C. Duan, Luminescent sensing and catalytic performances of a multifunctional Lanthanide-organic framework comprising a triphenylamine moiety, *Adv. Funct. Mater.* 2114 (2011) 2788-2794. <https://doi.org/10.1002/adfm.201100115>
- [29] G. Cai, P. Cui, W. Shi, S. Morris, S. N. Lou, J. Chen, J. H. Ciou, V. K. Paidi, K. S. Lee, S. Li, P. S. Lee, One-dimensional pi-d conjugated coordination polymer for electrochromic energy storage device with exceptionally high performance, *Adv. Sci.* 720 (2020) 1903109. <https://doi.org/10.1002/advs.201903109>
- [30] S. Zhou, S. Wang, S. Zhou, H. Xu, J. Zhao, J. Wang, Y. Li, An electrochromic supercapacitor based on an MOF derived hierarchical-porous NiO film, *Nanoscale* 1216 (2020) 8934-8941. <https://doi.org/10.1039/d0nr01152e>
- [31] C. R. Wade, M. Li, M. Dinca, Facile deposition of multicolored electrochromic metal-organic framework thin films, *Angew. Chem. Int. Edit.* 5250 (2013) 13377-13381.

<https://doi.org/10.1002/anie.201306162>

- [32] C. W. Kung, T. C. Wang, J. E. Mondloch, D. Fairen-Jimenez, D. M. Gardner, W. Bury, J. M. Klingsporn, J. C. Barnes, R. Van Duyne, J. F. Stoddart, M. R. Wasielewski, O. K. Farha, J. T. Hupp, Metal-organic framework thin films composed of free-standing acicular nanorods exhibiting reversible electrochromism, *Chem. Mat.* 2524 (2013) 5012-5017 (2013). <https://doi.org/10.1021/cm403726v>
- [33] I. Mjejri, C. M. Doherty, M. Rubio-Martinez, G. L. Drisko, A. Rougier, Double-sided electrochromic device based on metal-organic frameworks, *ACS Appl. Mater. Interfaces* 946 (2017) 39930-39934. <https://doi.org/10.1021/acsami.7b13647>
- [34] J. Liu, X. Y. Daphne Ma, Z. Wang, L. Xu, T. Xu, C. He, F. Wang, X. Lu, Highly stable and rapid switching electrochromic thin films based on metal-organic frameworks with redox-active triphenylamine ligands, *ACS Appl. Mater. Interfaces* 126 (2020) 7442-7450. <https://doi.org/10.1021/acsami.9b20388>
- [35] J. L. Hauser, M. Tso, K. Fitchmun, S. R. J. Oliver, Anodic electrodeposition of several metal-organic framework thin films on indium tin oxide glass, *Cryst. Growth Des.* 194 (2019) 2358-2365. <https://doi.org/10.1021/acs.cgd.9b00054>
- [36] B. Dhara, S. Sappati, S. K. Singh, S. Kurungot, P. Ghosh, N. Ballav, Coordination polymers of Fe(iii) and Al(iii) ions with TCA ligand: distinctive fluorescence, CO₂ uptake, redox-activity and oxygen evolution reaction, *Dalton Trans.* 4516 (2016) 6901-6908. <https://doi.org/10.1039/c6dt00009f>
- [37] D. Mohanadas, T. B.S.A. Ravooof, Y. Sulaiman, A fast switching electrochromic performance based on poly(3,4-ethylenedioxythiophene)-reduced graphene oxide/metal-organic framework HKUST-1, *Sol. Energy Mater. Sol. Cells* 214 (2020) 110596. <https://doi.org/10.1016/j.solmat.2020.110596>
- [38] K. Zhou, H. Wang, J. Jiu, J. Liu, H. Yan, K. Suganuma, Polyaniline films with modified nanostructure for bifunctional flexible multicolor electrochromic and supercapacitor applications, *Chem. Eng. J.* 345 (2018) 290-299. <https://doi.org/10.1016/j.cej.2018.03.175>
- [39] H. Qu, X. Zhang, H. Zhang, Y. Tian, N. Li, H. Lv, S. Hou, X. Li, J. Zhao, Y. Li, Highly robust and flexible WO₃·2H₂O/PEDOT films for improved electrochromic performance in near-infrared region, *Sol. Energy Mater. Sol. Cells* 163 (2017) 23-30. <http://dx.doi.org/10.1016/j.solmat.2016.12.030>
- [40] X. Mao, Y. Liu, Z. Chen, Y. Fan, P. Shen, Fe and Co dual-doped Ni₃S₄ nanosheet with enriched high-valence Ni sites for efficient oxygen evolution reaction, *Chem. Eng. J.* 427

- (2022) 130742. <https://doi.org/10.1016/j.cej.2021.130742>
- [41] W. Li, X. Zhang, X. Chen, Y. Zhao, L. Wang, M. Chen, J. Zhao, Y. Li, Y. Zhang, Effect of independently controllable electrolyte ion content on the performance of all-solid-state electrochromic devices, *Chem. Eng. J.* 398 (2020) 125628. <https://doi.org/10.1016/j.cej.2020.125628>
- [42] H. Y. Qu, D. Primetzhofer, M. A. Arvizu, Z. Qiu, U. Cindemir, C. G. Granqvist, G. A. Niklasson, Electrochemical rejuvenation of anodically coloring electrochromic nickel oxide thin films, *ACS Appl. Mater. Interfaces* 949 (2017) 42420-42424. <https://doi.org/10.1021/acsami.7b13815>
- [43] H. Y. Qu, X. Wang, D. Chen, Z. Bai, N. Wang, Y. Q. Zhu, Z. Tong, H. Ji, G. A. Niklasson, Cation-/anion-based physicochemical mechanisms for anodically-coloring electrochromic nickel oxide thin films, *ChemElectroChem* (2022) e202101503 <https://doi.org/10.1002/celec.202101503>
- [44] A. Kundu, A. Samanta, C. R. Raj, Hierarchical hollow MOF-derived bamboo-like N-doped carbon nanotube-encapsulated Co_{0.25}Ni_{0.75} alloy: An efficient bifunctional oxygen electrocatalyst for Zinc-Air battery, *ACS Appl. Mater. Interfaces* 1326 (2021) 30486-30496. <https://doi.org/10.1021/acsami.1c01875>
- [45] M. A. Arvizu, H. Y. Qu, U. Cindemir, Z. Qiu, E. A. Rojas-Gonzalez, D. Primetzhofer, C. G. Granqvist, L. Osterlund, G. A. Niklasson, Electrochromic WO₃ thin films attain unprecedented durability by potentiostatic pretreatment, *J. Mater. Chem. A* 76 (2019) 2908-2918. <https://doi.org/10.1039/c8ta09621j>
- [46] Z. Zhang, H. Gai, Q. Li, B. Feng, M. Xiao, T. Huang, H. Song, Effect anions on the hydrogenation of nitrobenzene over N-rich poly(ionic liquid) supported Pd catalyst, *Chem. Eng. J.* 429 (2022) 132224. <https://doi.org/2021.10.1016/j.cej.2021.132224>
- [47] Z. Peng, X. Yi, Z. Liu, J. Shang, D. Wang, Triphenylamine-based metal-organic frameworks as cathode materials in Lithium-ion batteries with coexistence of redox active sites, high working voltage, and high rate stability, *ACS Appl. Mater. Interfaces* 823 (2016) 14578-14585. <https://doi.org/10.1021/acsami.6b03418>
- [48] X. Tang, H. Wang, J. Fan, L. P. Lv, W. Sun, Y. Wang, CNT boosted two-dimensional flaky metal-organic nanosheets for superior lithium and potassium storage, *Chem. Eng. J.* 430 (2022) 133023. <https://doi.org/10.1016/j.cej.2021.133023>
- [49] G. H. Nishesh, K. Suho, B. Jiyeol, K. S. Kwang, Fabrication of Cu(BDC)_{0.5}(BDC-NH₂)_{0.5} metal-organic framework for superior H₂S removal at room temperature, *Chem. Eng. J.* 411 (2021) 128536. <https://doi.org/10.1016/j.cej.2021.128536>

- [50] D. Li, T. Liu, Z. Yan, L. Zhen, J. Liu, J. Wu, Y. Feng, MOF-derived Cu₂O/Cu nanospheres anchored in nitrogen-doped hollow porous carbon framework for increasing the selectivity and activity of electrochemical CO₂-to-formate conversion, *ACS Appl. Mater. Interfaces* 126 (2020) 7030-7037. <https://doi.org/10.1021/acsami.9b15685>
- [51] Y. An, M. Han, H. Zheng, W. Ding, Q. Sun, C. Hu, L. Zheng, Hollow structured copper-loaded self-floating catalyst in sulfite-induced oxidation of arsenic(III) at neutral pH: kinetics and mechanisms investigation, *Chem. Eng. J.* 407 (2021) 127193. <https://doi.org/10.1016/j.cej.2020.127193>
- [52] Y. Yuan, L. M. Sun, H. Gao, S. Mo, T. Xu, L. Yang, W. W. Zhan, Engineering a highly improved porous photocatalyst based on Cu₂O by a synergistic effect of cation doping of Zn and carbon layer coating, *Inorg. Chem.* 5921 (2020) 16010-16015. <https://doi.org/10.1021/acs.inorgchem.0c02547>
- [53] L. Wang, D. Jia, L. Yue, K. Zheng, A. Zhang, Q. Jia, J. Liu, In situ fabrication of a uniform Co-MOF shell coordinated with CoNiO₂ to enhance the energy storage capability of NiCo-LDH via vapor-phase growth, *ACS Appl. Mater. Interfaces* 1242 (2020) 47526-47538. <https://doi.org/10.1021/acsami.0c12759>